SPACE PROPULSION 2026
Bari, ITALY | 18 – 21 MAY 2026

Particle in Cell algorithm with azimuthal Fourier mode decomposition for the study of instabilities in cylindrical plasma sources

M. Ripoli[(1)], Eduardo Ahedo[(2)], Mario Merino[(3)]

Universidad Carlos III de Madrid, Leganés, 28911, Spain
[(1)] Ph.D. student, mripoli@ing.uc3m.es
[(2)] Full professor, eahedo@ing.uc3m.es
[(3)] Full professor, mario.merino@uc3m.es

KEYWORDS: Particle-in-Cell, space propulsion, plasma waves

ABSTRACT:

A numerical scheme to efficiently perform full-dimensional kinetic non-linear simulations of cylindrical plasmas is presented. Taking advantage of the cylindrical geometry of many plasma sources, a Fourier mode decomposition of the fields is carried out in the azimuthal (θ) direction. Then, a standard finite-difference Particle-in-Cell approach is used in the meridian plane for each azimuthal mode m. Particle weighing and field interpolation take into account all the spectral modes up to a chosen maximum m_{max}. The approach brings spectral accuracy in the azimuthal direction, while the computational cost is far lower than that of a full 3D-finite-difference scheme, roughly amounting to just m times a 2D simulation. The code is benchmarked against a test case widely used for validation purposes in the Low Temperature Plasma community based on a Penning discharge, and the advantages and pitfalls of the numerical scheme for electric propulsion applications are commented.

1. INTRODUCTION

Many plasma devices operate as partially magnetized $E \times B$ discharges, their applications ranging from material processing to space propulsion [1]. In this regime, electrons are well magnetized and closely follow magnetic field lines, whereas heavier ions are essentially unaffected by magnetic force effects. While the variety of devices is ample, they all share the physical working principles, acting as magnetically-confined plasma sources, as well as the susceptibility to wave-driven transport of charged species across magnetic field lines [2]. Magnetrons, Penning discharges [3, 4] and Hall Thrusters [5, 6, 7] all fall in this category, which also includes the under-development family of Electrodeless Plasma Thrusters (EPTs)[8, 9, 10, 11, 12, 13, 14], which rely on a magnetic nozzle (MN) [15, 16, 17, 18] as their accelerating stage.

Simulating these discharges efficiently is a topic of main interest for the low-temperature plasmas community, as the triggering and non-linear evolution of plasma instabilities remains an open problem in these devices. Linear wave excitation and unstable growth in collisionless partially magnetized plasmas has been dealt with frequently in the literature, both from fluid [19, 20, 21, 22] and kinetic [23, 24, 25] perspectives. These works highlight how interspecies drift, arising from the difference in magnetization between ions and electrons, acts as the main driver behind the insurgence of instabilities in $E \times B$ discharges. These phenomena can be categorized under the comprehensive list of collisionless *drift-gradient instabilities* whose most notable examples are the lower-hybrid drift instability (LHDI) [23, 26, 27] and its simplified zero-electron Larmor radius limit version [28], also known as the modified collisionless variant of the Simon-Hoh instability [29]. Some theoretical works have extended their analytical effort to describing the non-linear stage of the wave evolution under the hypothesis of weak turbulence, using quasi-linear models [30, 31, 22] and semi-heuristic saturation criteria [32] to quantify oscillation-driven transport and heating.

All these studies are however limited to weakly inhomogeneous plasmas and weak turbulence, failing to provide satisfying insight for global, highly non-linear time-varying phenomena in these discharges. For this reason, there is an ever-growing need to provide efficient and credible numerical integrations of the time-resolved nonlinear dynamics of electrostatic plasma discharges, capable of retaining at least part of the full 3D problem. While fluid approaches have been explored [33, 34], the full characterization of the plasma-wave interaction requires a kinetic framework, solving the non-linear kinetic equation for each one of the plasma species and to couple them through Poisson's equation. This

can be done numerically by means of the electrostatic Particle-In-Cell (PIC) method, where charged macroparticles are moved independently under the action of the background magnetic field and the time-varying electric potential [35, 36, 37, 38, 39].

Virtually all existing PIC codes compute the fields through finite differencing (FD) over all spatial dimensions on a grid and then interpolate them on the macroparticle position. Indeed, this is the Eulerian part of the PIC scheme. However, grid based methods scale onerously with the dimensionality of the problem. In addition, they lead to the well-known finite-grid instability [40] and to spurious heating, violating the energy balance for momentum-conserving codes. Energy preserving schemes have been employed to overcome these problems [41, 42].

Given the large computational times that come with the standard PIC method in 3D, most of the analyses are usually limited to 2D problems. Many 2D PIC codes have been used to study cylindrical discharges, restricting their analyses only to axial-azimuthal [43, 44, 39] or axial-radial [45, 46] sections of the real device. Yet many other works explore only the axisymmetric part of the plasma response, by integrating the axial-radial plane of the source, ignoring or externally modeling any azimuthal fluctuations [47, 48, 49, 50, 36, 51, 52].

Interestingly, the vast majority of $E\times B$ plasma devices possess a cylindrical geometry, a fact that can be exploited to establish a more efficient (and accurate) simulation scheme for the 3D problem than gridding over all three spatial dimensions. Indeed, by Fourier-expanding in the azimuthal direction θ the fields that are traditionally defined over the 3D grid (electrostatic potential and field; electron and ion density and current; higher moments of the distribution functions), it is possible to approach the simulation of the full problem by solving separately each of the azimuthal modes m up to a desired truncation mode number N_m in a 2D grid in the axial-radial directions. While macroparticles must be pushed in 3D space, their weighting in the azimuthal direction is carried out by projecting their density onto the Fourier basis in θ. Their weighting in the axial and radial directions can continue to be carried out on a 2D grid using FD, as this offers higher flexibility to deal with complex boundary conditions. The solution of each mode of the electrostatic potential, ϕ^m, requires solving a separate 2D Poisson problem with the corresponding mode of the charge density, $q(n_i^m - n_e^m)$. The 3D electrostatic field is readily constructed from the 2D contribution of each mode to push the macroparticles in the next time step. This concept is not new, and has been successfully used in other areas of plasma physics, e.g. to analyze laser-plasma interactions, where it has been termed the Particle-In-Fourier (PIF) method or simply spectral PIC [53, 54, 55, 56, 57]. However, to the best of our knowledge, it has not been employed in the field of electric propulsion.

Crucially, the number of modes of interest N_m in practical problems is usually small. Indeed, all studies based on axial-radial simulations, such as those referenced above, merely investigate the axisymmetric plasma source response (i.e., the mode $m = 0$). Moreover, many plasma fluctuations, like rotating spokes, can be effectively described with a few azimuthal modes, say < 100. Furthermore, the total number of macroparticles needed for an accurate simulation depends only on the axial-radial grid resolution and the number of azimuthal modes N_m. All this means that this approach has potential to accelerate the computation of the full solution of the problem compared to traditional 3D PIC. In addition, another advantage of the Fourier treatment of the azimuthal dimension, is the spectral accuracy of the method, and is the elimination of finite grid instabilities and other grid-related numerical phenomena [55] (if only in the θ direction). Last but not least, it is worth noting that when analyzing standard PIC simulation results, one often determines a posteriori the Fourier modes of the solution to discuss their specific behavior; the presented approach directly yields the modal amplitudes, as these are the quantities employed in the computation.

This work explores and discusses the simulation approach based on this concept as outlined above. We present a mixed PIC/PIF architecture, derived as an alternative to our full PIC code `PICASO`. Rather than tackling a 3D problem as a collection of 2D problems, the new scheme is used to simulate the cross sectional plane of a cylindrical discharge—a Penning source,—employing a spectral Fourier mode discretization in the azimuthal direction and regular finite differencing (FD) in the radial direction (1D+1F). This serves to illustrate the discretization process and analyze the advantages of the algorithm, but also as a first step toward the treatment of 3D problems using a grid in (z, r) and modal decomposition in θ (1F+2D). An additional advantage of this choice is that robust numerical studies exist in the literature on the convergence and benchmarking of the simulation of a Penning discharge, which allows us to compare the new algorithm directly against the traditional PIC approach.

The rest of the paper is structured as follows: in Section 2 the main features of the 2D Penning discharge problem are described. In Section 3 the model of the 1D+1F scheme is presented: at the end of the Section, the code implementation is discussed as well. In Section 4, simulation results with $N_m = 10$ are presented and discussed. At the end of this section, we compare against a recent benchmarking effort of the low-temperature plasma community for validating and comparing electrostatic PIC codes [58]. In section 5, a sensitivity analyses on the effect of numerical parameters is performed. Section 6 presents the conclusions of this work.

2. PROBLEM DESCRIPTION

Our model Penning discharge is a cylinder of radius $r = R$, and we consider a radial-azimuthal cross-section as displayed in the left side of figure 1. Different amounts of electrons and ions per unit time, I_{e0}, I_{i0}, are injected in the central region ($r \leq r_{inj}$). The injection profile follows a Heaviside function:

$$\dot{n}_s = \begin{cases} \dfrac{I_{s0}}{q_s \pi r_{inj}^2} & \text{for} \quad r \leq r_{inj} \\ 0 & \text{otherwise,} \end{cases} \tag{1}$$

with $s = e, i$. A uniform magnetic field B is applied in the axial direction (i.e., perpendicular to the plane of the cross section). The outer edge of the domain is set to a constant potential $\phi = 0$. No collisions are modeled in this work, and any macroparticles reaching the outer edge is eliminated from the simulation. Initially, the domain is empty. After a fill-up transient, the simulation evolves toward a quasi-steady regime, which presents a rotating spoke.

The upper part of table 1 lists the physical parameters of the simulation. The same physical parameters have been used for the benchmark study presented in [58]. Differently from that work, which employs a square geometry at the boundary, our domain is circular.

3. MODEL AND NUMERICAL IMPLEMENTATION

Our model extends the existing `PICASO` code to include the decomposition into azimuthal Fourier modes. `PICASO` is an explicit momentum-conserving PIC code which has been successfully applied to the study of space thruster plumes and plasma sources in a variety of 2D configurations, mainly in the axial-azimuthal plane [39, 59] and in axisymmetric cylindrical coordinates [36, 60, 61]. Recently, it has been benchmarked against similar PIC codes in a standardized test case [58]. The code is written in FORTRAN and is parallelized on CPU with OpenMP using a standard particle decomposition strategy. It makes use of the PARDISO MKL [62] library for solving the sparse Laplacian matrices of Eq. (4).

The distribution functions of ions and electrons are discretized using markers, or macroparticles, of constant weight w_p. Knowing the two dimensional electric field $\boldsymbol{E}$ and the applied axial magnetic field $\boldsymbol{B}$, an explicit Boris leapfrog scheme as the one outlined in [63] is used to push the macroparticles, which projects positions and velocities in a local Cartesian (x, y, v_x, v_y, v_z) coordinate system, updates them at staggered time and converts them back to cylindrical coordinates $(r, \theta, v_r, v_\theta, v_z)$. Note that, being the problem 2D, the effect of v_z on the position is inconsequential.

The radial-azimuthal maps of the ion and electron densities (and, similarly, any other moment of their distributions, and any other grid function like the electrostatic potential ϕ below) are decomposed into their azimuthal Fourier modes up to a truncation mode N_m as

$$n_s(r, \theta, t) = \Re \left[\sum_{m=0}^{N_m} n_s^m(r, t) \exp(im\theta) \right] \tag{2}$$

with $s = i, e$, and n_s^m the complex magnitude of mode m; note that this decomposition takes into account that the complex magnitude of positive and negative m modes are complex conjugate of each other to reduce the sum to only non-negative modes, which implicitly introduces a factor 2 in the definition of modes $m > 0$. This decomposition isolates the axisymmetric part of the densities n_s^0 from their non-symmetric part, and it elegantly represents rotating modes. For example, a simple $m = 1$ rotating spoke is characterized by a constant real magnitude $|n_s^1|$ and a complex phase $\angle n_s^1$ that evolves linearly in time. In reality, rotating structures can be more intricate, e.g. the real magnitude $|n_s^1|$ may vary in time in a quasi-periodic or even chaotic way, the phase may also have more sophisticated dynamics, and modes may be nonlinearly coupled together.

To compute the n_s^m functions, macroparticles of ions and electrons are weighted onto an equispaced r grid for each Fourier mode in θ, as represented in the right side of figure 1. In the radial direction, weighting is performed at the grid nodes r_i through the Cloud-in-Cell (CIC) method [35, 64], using a linear shape function S_r for macroparticle weighting on the nodes [35]. In the azimuthal direction, the contribution of each macroparticle the the m-th mode of the corresponding density map (n_i^m, n_e^m) is computed by projecting its position and weight onto the m-th Fourier mode. A Dirac delta shape function S_θ is employed in this projection; other, smoother shape function choices would be possible, to introduce some filtering at higher azimuthal modes, but they are not explored in the present work. All in all, the m-th mode of the density of species $s = i, e$ at the radial node r_i is computed as

$$\begin{aligned} n_s^0(r_i) &= \sum_{p \in s} \frac{w_p}{4\pi^2 r_i \Delta r} S_r(r_p, r_i), \\ n_s^m(r_i) &= \sum_{p \in s} \frac{w_p}{2\pi^2 r_i \Delta r} S_r(r_p, r_i) \exp(-im\theta_p) \quad \text{for } m > 0, \end{aligned} \tag{3}$$

where the factor 2 in the definition of modes $m > 0$ has been taken into account.

To update the electric field $\boldsymbol{E}$ for the next time step, the Poisson equation needs to be solved. Given its linearity, each m-th mode of the electrostatic potential ϕ can then be obtained independently from the others as

$$\nabla^2 \phi^m \equiv \frac{1}{r} \frac{\partial}{\partial r} \left(r \frac{\partial \phi^m}{\partial r} \right) - \frac{m^2}{r^2} \phi^m = \frac{q(n_i^m - n_e^m)}{\varepsilon_0} \tag{4}$$

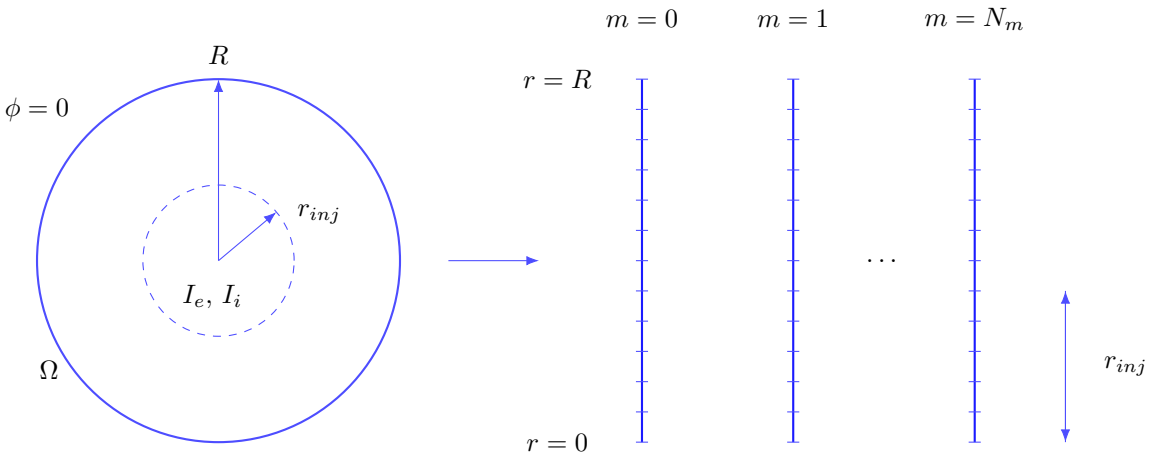


Figure 1. Geometry of the problem (left) and schematization of the 1D+1F scheme as a series of $2N_m + 1$ uncoupled $1D$ problems (right).

Physical parameter	**Symbol**	**Value**	**Unit**
Helium-4 ion mass	m_i	7291.2	m_e
Domain radius	R	2.5	cm
Injection radius	r_{inj}	0.5	cm
Electron injection current	$I_{e,0}$	-20×10^{-3}	A/m
Electron injection temperature	T_e	15	eV
Ion injection current	$I_{i,0}$	8×10^{-3}	A/m
Ion injection temperature	T_i	0.025	eV
Applied magnetic field strength	B	0.1	T
Numerical parameter	**Symbol**	**Value**	**Unit**
Time step size	Δt	0.04	ns
Number of time steps	N_{sim}	1.25×10^7	-
Total simulation time	t_{sim}	500	μs
Steps between diagnostic print	N_{print}	1.25×10^4	-
Time between diagnostic print	Δt_{print}	0.5	μs
Cells in r direction	N_r	128	-
Cell size	Δr	0.02	cm
Macroparticle weight	w_p	8.25×10^6	particles
Number of modes	N_m	10	-

Table 1. Simulation parameters for the Penning discharge (reference case).

where ε_0 is the (unmodified) electric permittivity in vacuum. The electric field can then be reconstructed simply as

$$\boldsymbol{E} = \Re\left[\sum_{m=0}^{N_m}\left(\frac{\partial\phi^m}{\partial r}\mathbf{1}_r + \frac{im}{r}\phi^m\mathbf{1}_\theta\right)\exp(im\theta)\right]. \quad (5)$$

The derivatives along r appearing in equations (4) and (5) are evaluated via centered FD. While a staggered grid scheme offers several advantages, in the present implementation both ϕ and $\boldsymbol{E}$ are computed at the grid nodes r_i.

Finally, the field $\boldsymbol{E}$ is interpolated at the macroparticle positions. While expression (5) is continuous in θ and therefore can be directly evaluated at the macroparticle azimuthal position θ_p, in the radial direction we interpolate using the same radial shape function S_r, employing the value of $\boldsymbol{E}$ at neighboring grid points.

The numerical parameters for the reference simulation discussed in section 4 are displayed in the second half of table 1. Regarding the implementation details, while equation (4) has to be solved $2N_m + 1$ times, the use of direct-iterative preconditioning to the sparse Laplace matrix renders the time to solve the entire system of Poisson's equation a small fraction of the total computational time. Elementary recursive formulas are used to speed up the computation of the transcendental functions of θ_p appearing in the weighting, equation (3), and in the evaluation of the electric field at the macroparticle's azimuth, equation (5).

3.1. Particle injection

Particle injection takes place in the core region $r < r_{inj}$. The coordinates of newly injected macroparticles are given by sampling two random numbers uniformly distributed between 0 and 1, $x_1, x_2 \sim \mathcal{U}(0,1)$, so that

$$r_p = r_{inj}\sqrt{x_1}, \qquad \theta_p = 2\pi x_2. \quad (6)$$

This provides an axisymmetric injection in the domain. Macroparticles are injected following a maxwellian distribution in velocity space with species-specific temperature T_s and zero fluid velocity.

The chosen values of the injection currents I_e, I_i, the time step Δt, and the macroparticle weight w_p mean that a noninteger number of macroparticles needs to be injected every time step, exceeding an integer number by a fractional reminder. To resolve this circumstance, each time step an additional random number is drawn and compared against the fractional remainder. If the fractional remainder is larger than the random number, an additional macroparticle is injected, otherwise the fractional remainder is accumulated to the number of macroparticles to be injected at the next step.

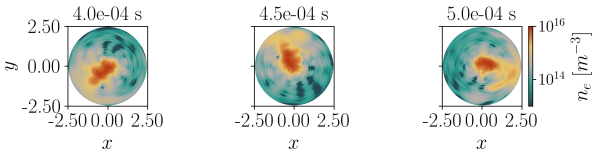


Figure 2. 2D representation of the time evolution of the rotating spoke at different instants for the reference case $N_m = 10$.

3.2. Boundary conditions

The outer boundary of the domain, indicated as Ω, is treated as a perfect grounded conductor, imposing on the potential the Dirichlet condition for all modes m

$$\phi^m|_{r=R} = 0; \quad (7)$$

the boundary Ω corresponds in the 1D+1F scheme to setting $r = R$, with R the radius of the domain.

The boundary condition at the axis, in contrast, differs for the axisymmetric mode ($m = 0$) and the non-symmetric modes ($m > 0$). Geometric consistency demands that ϕ^0 have null radial derivative at the axis to avoid E_r^0 to be ill-defined at the centre of the circular domain, yielding

$$\left.\frac{\partial\phi^0}{\partial r}\right|_{r=0} = 0. \quad (8)$$

For all other modes, any dependence on θ should vanish at the axis, which imposes the same homogeneous Dirichlet condition,

$$\phi^m|_{r=0} = 0 \quad \text{for } m > 0. \quad (9)$$

Regarding the boundary conditions on the macroparticles, any macroparticles reaching the outer domain radius are removed from the simulation. No boundary condition on the macroparticles is needed at the axis, where the macroparticle kinematics and dynamics are consistently solved.

4. RESULTS

Here the main results of the reference Penning discharge simulation with $N_m = 10$ are presented. A few 2D snapshots of the electron density after the initial transient setup, reconstructed using equation (2), are shown in 2. A coherent and stable anticlockwise rotating spoke structure is recovered, as expected in this parametric regime [58]. The spoke rotates in the $\boldsymbol{E} \times \boldsymbol{B}$ direction. Except in a thin sheath around the outer boundary, the plasma remains essentially quasineutral everywhere.

Figure 3 presents the long-time averages and standard deviations of the radial profiles of the first modes of $|n_e^m|$, $|\phi^m|$ and $|E_\theta^m|$, i.e., the absolute value of the mode amplitudes (that is, stripped of their complex phase). For reference, the injection region and the Debye and Larmor lengths at the

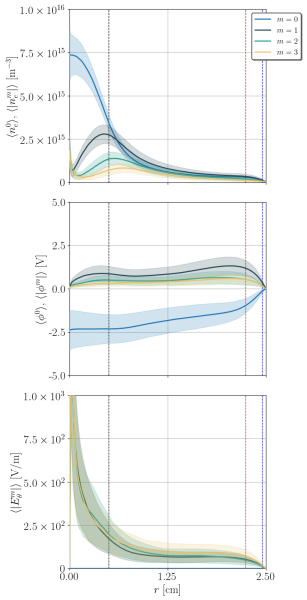


Figure 3. Long-time averages and standard deviations of the absolute value of the modal components $|n_e^m|$, $|\phi^m|$ and $|E_\theta^m|$ for $m = 0, 1, 2, 3$, for the reference simulation with $N_m = 10$. Mode $m = 0$ has a real amplitude (i.e. no complex phase), and in the case of ϕ, its signed profile is shown. The statistics have been carried over the last 500 diagnostic prints, each of them spaced by 12500 timesteps, and therefore are representative of the last 250 μs. Solid lines correspond to mean values, while the half widths of the shaded areas represent the amplitude of the associated standard deviation. The dashed black vertical line denotes $r = r_{inj}$; red indicates a Debye thickness from the boundary, $r = R - \lambda_{De}$; blue a Larmor thickness, $r = R - \rho_e$.

outer wall are represented. Mode $m = 0$ has a real amplitude (i.e. no complex phase), and in the case of ϕ, its signed profile is shown. The statistics are computed rejecting the transient setup part of the simulation. The standard deviation is indicative not only of the noise in the simulation (which scales as $1/\sqrt{N_p}$, with N_p the number of macroparticles per cell), but also of the physical oscillations of each mode over time.

The 0th mode, i.e. the axisymmetric plasma response, exhibits a centered peak in density n_e and a shallow well of the potential ϕ. This is consistent with a Penning discharge with $I_e > I_i$, where a negative radial electric field $E_r < 0$ acts to push out the excess electrons and confines the lower amount of ions at steady state, where the currents reaching the outer wall are in average the same as the injection currents. Interestingly, the height of the density peak (and also the depth of the potential well) are strongly dependent on the strength of the effective radial transport of the otherwise well-magnetized electrons. As we show next, higher modes $m > 0$ (and specially $m = 1$) are essential in setting up the radial $E \times B$ transport mechanism that enables the injected I_e to eventually reach the boundary. Indeed, our experiments with $N_m = 0$ (i.e., where we simulate only the axisymmetric response) yield a much higher peak of n_e, and a steady state is only reached when the stochastic oscillations due to PIC noise in ϕ become large enough to provide a numerical conductivity for the electrons.

The first non-symmetric modes $m = 1, 2, 3$ have an electron density n_e that peaks at some intermediate radius r, which increases with m. The absolute value of the modes of the electrostatic potential ϕ is nonzero and essentially flat, with mild peaks near the axis and the boundary (prior to one Debye length of it). While not explicitly shown here, the relative phase of n_e^m and ϕ^m is such that, on average, each mode contributes to set up the expected $E \times B$ transport in the radially-outward direction.

A crucial feature of the mode amplitudes is that they all decrease with m roughly as $1/m$. In contrast, the modes of the azimuthal electric field $|E_\theta^m|$ remains almost constant with m, since

$$|E_\theta^m| = \frac{m}{r}|\phi^m|. \tag{10}$$

Fortunately, the induced radial transport contributed by each mode (which roughly scales with $n_e^m E_\theta^m$) does decay with m. Quickly-decaying modes are essential to truncate the modal expansion at a moderate N_m for computational efficiency; the fact that $|E_\theta^m|$ does not appear to vanish with m calls for caution and a thorough sensitivity analysis to find an adequate value of N_m to retain all the modes of importance for the plasma dynamics. This is further discussed in section 5.

Incidentally, while at the boundary $\phi \to 0$, the modes of n_e and ϕ do not exactly vanish; this is an artifact of numerical noise and the fact that we are averaging $|n_e^m|$, $|\phi^m|$, and not the full complex magnitudes (whose average does go to zero).

We can gain some insight into the dynamics of the spoke by additionally Fourier-expanding each mode in time. Each modal coefficient in equation (2) can be expressed in the frequency domain as

$$n_e^m(r,t) = \frac{1}{N_t}\sum_{n=0}^{N_t-1} n_e^{m,n}(r)\exp\left(-i\omega^n t\right) \tag{11}$$

with $\omega^n = 2\pi n/(N_t \Delta t_{print})$ the discrete n-th frequency, and N_t is the number of print steps. Now we must retain both positive and negative frequencies, as n_e^m is complex (with the exception for $m = 0$, which has a symmetric time spectrum).

Figure 4 presents the normalized PSD of n_e^m domain at two radial positions, $r = 1.66$ cm and close to the boundary, $r \simeq R = 2.5$ cm. The normalization has been carried out using as a reference the maximum overall PSD value, which takes place for the $m = 1$ mode at approximately $\omega_{max,1} = 52.21$ kHz. It is evident that the PSD peaks on a diagonal line with a single phase velocity, $v_{ph} = r\omega/m$,

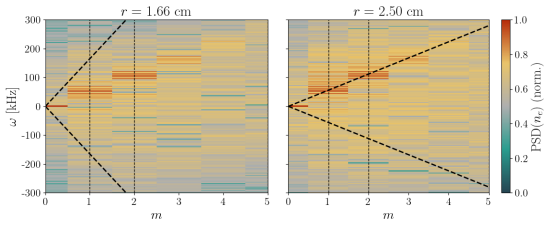


Figure 4. PSD of n_e^m for the first azimuthal modes of the reference simulation at two radial positions. The time window and number of timesteps used to compute the PSD are the same as those used in the long-time averaging of figure 3. Values have been normalized with respect to the peak PSD value overall. The black lines indicate the averaged sonic velocity, $\pm\langle c_s\rangle$.

consistent with a rotating spoke. At the edge of the domain, $v_{\theta,ph}$ matches the ion sound velocity there, $c_s = (T_e^0/m_i)^{1/2}$, indicating that the spoke is a sonic-like structure. T_e is the locally computed perpendicular electron temperature. The PSD of ϕ (and therefore E_θ) display the same structure, revealing that the electrostatic potential follows the same dynamcics as the density spoke.

Incidentally, the spectrum in figure 4 also reveals another interesting feature of the simulation. While the spectrum of each mode n_e^m displays a clear peak, there is non-negligible spectral content at other frequencies too. This is an indication that the absolute value of the modal amplitudes does not reach a steady-state profile, but rather, present small oscillations about their average profiles in figure 3. These oscillations occur over a slow time scale (corresponding to the frequencies in the spectrum), and clearly differ from statistical noise oscillations. Indeed, our investigations show that a short-time average with a small Δt has a much narrower standard deviation (which in this case comes solely from noise) than those displayed in figure 3 (which represent mainly the physical, slow oscillations of the modes). Further analysis shall look into the dynamics of each mode, and identify potential nonlinear couplings across modes, employing the techniques used in [59].

4.0.1 Benchmark

The reference simulation was carried out with the same physical parameters as in the community benchmark [58] to facilitate comparison. In that work, the same Penning discharge simulation was computed by different groups using different 2D PIC codes, showing great agreement. Figure 5 displays the mean and the variability across those benchmark simulations for the axisymmetric profiles n_e^0, n_i^0, ϕ^0 and T_e^0. In this figure, and for comparison, the long-time average and standard deviation of our 1D+1F simulation for these variables is also included.

Our simulation shows an overall good match with the benchmark, especially in the potential and in the perpendicular electron temperature profiles. The most striking difference is the discrepancy in the density profiles, which have essentially the same structure but differ by a factor of about 1.2. The average density profile depends strongly on the effective radial transport coefficient, and therefore, this difference can be interpreted as our 1D+1F simulation having a slightly lower transport. An additional discrepancy is related to the spoke frequency, measured as 52.21 kHz from the PSD of Fig. 4, while in the benchmark case it has been computed as 44.35 kHz. There are several potential reasons to explain these divergences. A first noteworthy difference between the benchmark simulations and our own is that the former all use a square domain, whereas in our work the domain is intrinsically cylindrical. This is by no means a small change in the simulation setup, as in each case the rotating structures encounter a different boundary condition at the wall of the Penning source, and this can have an impact on the resulting profiles. The difference in spoke frequency likely stems from this: as observed before, the spoke coincides with the sonic wave exactly at the edge of the domain in our 1D+1F simulation, and very likely the phase velocity in the benchmark simulation is also dependant on the boundary configuration, too. Secondly, the macroparticles and the underlying grids have different shapes in the two schemes. As a result, the two codes likely experience noise and numerical diffusion differently. Arguably, our radial grid + azimuthal modes approach is better aligned with the principal transport directions (radial, azimuthal) than a square grid, which suggests the possibility of a lower numerical diffusion in the 1D+1F case. This, however, remains to be investigated and ascertained. Thirdly, the total number of macroparticles, and the macroparticles per cell N_p, differ too. The latter numerical parameter, which is larger in our simulation, has a dominant role in the noise statistics, which can influence numerical transport. Finally, we are intentionally truncating the azimuthal modal expansion in the reference simulation at $N_m = 10$, whereas the benchmark simulation can tackle much finer azimuthal structures, limited by the 2D mesh resolution.

While the former two aspects are inherent differences of the two approaches, the latter two aspects are investigated further in section 5 next.

5. CONVERGENCE ANALYSIS AND PERFORMANCE ASSESSMENT

In this section we compare different simulations changing maximum number of modes N_m and macroparticle weight w_p with respect to the reference case, which indirectly determines the number of macroparticles per cell N_p. The purpose is to determine how the resulting profiles differ from the ref-

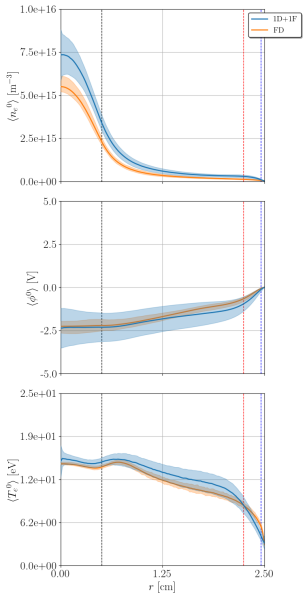


Figure 5. Comparison between long-time averaged radial profiles of the reference 1D+1F simulation (blue) with $N_m = 10$ and those from [58] (orange). The orange shaded area describes the variability among all the different PIC codes listed in that paper. Vertical dashed lines are as in figure 3.

Case	N_m	w_p	Δt [ns]	Δr [cm]
Reference	10	8.25×10^6	4×10^{-2}	0.02
S1	5	8.25×10^6	4×10^{-2}	0.02
S2	20	8.25×10^6	4×10^{-2}	0.02
S3	20	8.25×10^6	2×10^{-2}	0.01
S4	10	1.65×10^7	4×10^{-2}	0.02
S5	10	4.125×10^6	4×10^{-2}	0.02

Table 2. Additional simulation cases and their respective numerical parameters for the convergence analysis.

erence case and the benchmark of [58], in the light of their computational cost. A total of 5 additional different simulation cases, differing from the reference detailed in Table 1, are listed in Table 2. Simulations S1 and S2 explore the effect of varying N_m. Simulation S3 is a variation of S2, where we have halved the timestep Δt and the grid size Δr. Simulation S4 and S5 explore the effect of varying w_p and consequently N_p.

The maximum number of simulated modes N_m influences radial transport and affects the average plasma profiles. The left side of figure 6 displays the axisymmetric part of the plasma response for simulations S1, S2 and S3. Intuitively, including more modes in the simulation enables additional channels for $E \times B$ transport to develop, and this results in a lower density n_e. Indeed, while the lowest nonzero modes are the largest contributors to transport, higher modes can also bring in an additional input to it. This is observed when increasing N_m

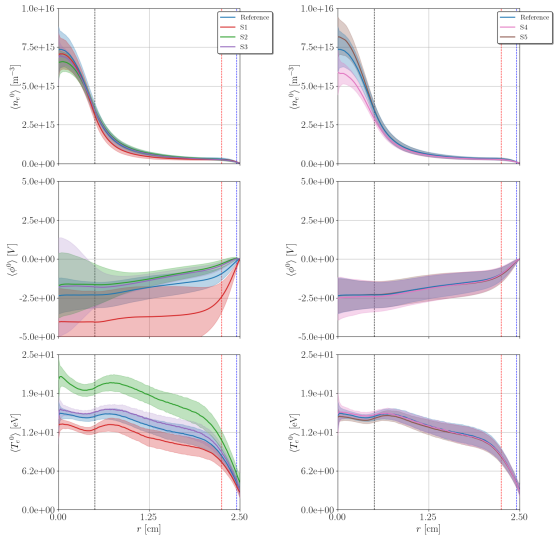


Figure 6. Comparison between long-time averaged radial profiles and respective standard deviations between the reference simulation case and cases S1, S2, S3 (left) and S4, S5 (right). Vertical dashed lines are as in figure 3.

from 10 (Reference) to 20 (S2). An additional test with $N_m = 0$ (not shown) proved that in the absence of azimuthal structures and therefore $E \times B$ radial transport, the density profile reached much higher values. Furthermore, the monotonic trends of the potential ϕ or the temperature T_e in the sequence S1→Reference→S2 indicate that as more modes are included, less radial electric field (and less oscillations in it) is needed at steady state, as the $E \times B$ mechanism enhances the electron transport to the wall. These results also show that electrons appear to heat up more as the simulation treats additional modes.

Nevertheless, our findings also show that the differences in density n_e between $N_m = 5$ (S1) and 10 (Reference), while small, hint at a slightly lower density peak in S1, which suggests a more sophisticated influence of the choice of N_m on transport and n_e. Indeed, the average density profile emanates not only from the $E \times B$ transport induced by the rotating azimuthal structures, but also from the interplay with the radial electrostatic field E_r and its fluctuations in time. These become larger the lower N_m, as illustrated by the S1 simulation. In addition, azimuthal modes are likely nonlinearly coupled, and their overall dynamics may depend on the number of simulated modes.

The choice of Δt and Δr can also affect the simulation results. For brevity, only the simulation S3 is shown in this work, which halves these quantities with respect to S2. Note that, in doing so, the number of particles per cell is also roughly halved. As can be observed in figure 6, this change brings the profiles back closer to the Reference case. Additional tests (not shown) showed that the extent of the effect on the profiles of modifying Δt and Δr de-

CPUs	t_{wall}	SF
$20\times$ Intel Xeon Gold 6542Y	2d 4h	1
$20\times$ Intel Xeon Silver 4316	2d 6h	0.83
$20\times$ Intel Xeon Gold 6230	2d 17h	0.79

Table 3. Scaling factor (SF) used to normalize the wall time t_{wall} of each machine, obtained by running the same simulation S4 on all of them.

Case	t^*_{wall}	Total macroparticles
Reference	4d 7h	$3.34 \cdot 10^5$
S1	5d 17h	$2.84 \cdot 10^5$
S2	7d 15h	$3.40 \cdot 10^5$
S4	1d 19h	$1.45 \cdot 10^5$
S5	8d 23h	$6.74 \cdot 10^5$
2D PICASO	16d 18h	$\simeq 10^7$

Table 4. Normalized computational time and total number of macroparticles for the different simulation cases. Times have been rescaled accounting for hardware differences as reported in table 3.

pends on N_m.

The influence of PIC noise on transport is quite apparent when comparing cases with different macroparticle weight. The right half of 6 shows simulations S4 and S5, which respectively double and halve the macroparticle weight w_p. The sequence S4→Reference→S5 goes toward finer particles with smaller w_p (and therefore a larger N_p). Increasing the marcroparticle count has the net effect of leading to a higher density peak; however, the profiles of potential ϕ and electron temperature T_e are essentially unaffected by this numerical parameter. Incidentally, the worse resolution in S4 closely matches the density profile of [58].

The $m = 1$ spoke frequency for the S1 case is computed to be 80.32 kHz, higher than for the reference, while for S2 the frequency is computed to be 52.21 kHz, exactly as for the reference case. For S3 the frequency peak is found 56.22 kHz. The spoke frequency for S4 is measured at 60 kHz while it remains at 52.21 kHz moving from the reference to S5.

As evidenced by figure 6, work is still required to characterize the convergence of the 1D+1F method. This reduces to determining safe values or ranges of N_m, w_p, Δt, Δr for which all aspects of the solution converge asymptotically and at what rate. This information would allow to make an informed decision on these parameters in the context of an accuracy-computational cost trade-off.

5.1. Computational cost

The simulations for the different cases have been run on different CPUs, and therefore need to be normalized to compare their computational cost. To this end, we ran the same simulation S4 on each machine, clocking the wall time t_{wall} to extract a scaling factor (SF), which was then used to normalize the rest of the simulations. This SF is reported in Table 3.

Table 4 presents the performance, in normalized wall time t^*_{wall}, between the various 1D+1F simulations of the Penning discharge (varying number of modes and macroparticle weight) and that of the standard FD scheme of the unmodified 2D PICASO code.

Aside from a clear scaling in the number of macroparticles, with t^*_{wall} scaling almost linearly with the number of macroparticles – see the comparison between the reference, S4 and S5 – there is a weaker scaling with the number of modes. It is notable that S4, which resembles closely the profiles form the FD code, needs $1/10$ of the total time that the FD codes requires. Note that, while S4 has way less partciles than FD ($1/100$), it computes $O(N_m)$ times the same $1D$ problem, which is more or less equivalent to having $O(N_m N_p)$ macroparticles. The case S3 has been omitted from the table, since it experiences a longer transient therefore not being fairly comparable in terms of runtime.

Aside from an anomalously large runtime in S1 – probably due to other processes running in parallel with the simulation, affecting its final runtime – t^*_{wall} scales *linearly* with N_p, as expected for any PIC code, while it scales in N_m following a *linear-with-offset* law. The offset is probably due to the first, costly evaluation of $\exp(i\theta_p)$, while for all other modes $m > 1$ the use of recursive relations lowers the cost for spectral weighting.

6. CONCLUSIONS

In this work we have presented Fourier-decomposed Particle-in-cell to study azimuthal features of cylindrical plasma discharges, and have applied to a Penning discharge to illustrate its performance. Our treatment expands all grid functions (fields, densities, higher moments of the distributions) in Fourier modes in the azimuthal direction, while it retains a grid in the remaining directions. Particle pushing and weighting remains full-dimensional. The modal decomposition in the azimuthal direction naturally exploits the cylindrical geometry of the source, provides spectral accuracy in this direction, and brings in the possibility truncating the computation at a chosen number of modes N_m, potentially resulting in computational savings with respect to traditional full-finite-differencing PIC. The gridded treatment in the remaining directions facilitates the imposition of complex boundary conditions, not easily done if a spectral treatment were to be applied also to them.

The 1D+1Fsimulation of the Penning discharge displays the well-known density spoke, which rotates with the characteristic sonic velocity. The axisymmetric mode $m = 0$ displays a bell-shaped plasma density profile, and a slight potential well as

expected. Modes $m > 0$ decay as $1/m$ and have a single-peaked yet broad frequency spectrum. In spite of the domain shape differences, reasonable agreement is found between our model and the community benchmark results of [58].

We have preliminarily explored the influence of the total number of azimuthal modes N_m and particle count N_p on the overall cross-field transport and the computational time. Increased transport is observed roughly when N_m is increased (more channels for $E \times B$ radial transport to develop) and N_p is lowered (higher statistical noise). While a full understanding of the convergence of the method will be part of future work, the potential advantages (in terms of computational time) of the 1D+1F approach have been evidenced. All in all, the 1D+1F (and its extension to 1F+2D) is an interesting alternative to classical FD schemes in the study of space plasma thrusters and other cylindrical plasma sources.

Improvements of the present approach are possible. A non-Uniform fast Fourier transform (NUFFT) [54, 65] could speed up the azimuthal weighting of the macroparticles into the modes, which our unoptimized version of the code does not consider yet. Pseudospectral approaches may also offer a valuable trade-off: a similar architecture has been presented in [64], differing from the one presented here for the presence of a grid in the azimuthal direction for particle weighting.

ACKNOWLEDGMENTS

This project has received funding from the European Research Council (ERC) under the European Union's Horizon 2020 research and innovation programme (Starting Grant project ZARATHUSTRA, grant agreement No 950466). Additional support came from the R&D project PID2023-150052OB-I00 (ADAPT) funded by MICIU/AEI/ 10.13039/ 501100011033 and by ERDF, EU.

REFERENCES

[1] J.-P. Boeuf and A. Smolyakov, "Physics and instabilities of low-temperature E x B plasmas for spacecraft propulsion and other applications," *Physics of Plasmas*, vol. 30, no. 5, p. 050901, 2023.

[2] I. D. Kaganovich, A. Smolyakov, Y. Raitses, E. Ahedo, I. G. Mikellides, B. Jorns, F. Taccogna, R. Gueroult, S. Tsikata, A. Bourdon, J.-P. Boeuf, M. Keidar, A. T. Powis, M. Merino, M. Cappelli, K. Hara, J. A. Carlsson, N. J. Fisch, P. Chabert, I. Schweigert, T. ahed-Lafleur, K. Matyash, A. V. Khrabrov, R. W. Boswell, and A. Fruchtman, "Perspectives on physics of E×B discharges relevant to plasma propulsion and similar technologies," *Physics of Plasmas*, vol. 27, no. 12, pp. 120–601, 2020.

[3] M. Druyvesteyn and F. M. Penning, "The mechanism of electrical discharges in gases of low pressure," *Reviews of Modern Physics*, vol. 12, no. 2, p. 87, 1940.

[4] F. C. Hoh, "Instability of Penning-type discharges," *The Physics of Fluids*, vol. 6, no. 8, pp. 1184–1191, 1963.

[5] H. Kaufman, "Technology of closed-drift thrusters," *AIAA Journal*, vol. 23, pp. 78–87, 1985.

[6] D. Goebel, I. Katz, and I. Mikellides, *Fundamentals of electric propulsion*. John Wiley & Sons, 2023.

[7] E. Ahedo, "Plasmas for space propulsion," *Plasma Physics and Controlled Fusion*, vol. 53, no. 12, p. 124037, 2011.

[8] C. Charles, R. Boswell, and M. Lieberman, "Xenon ion beam characterization in a helicon double layer thruster," *Applied Physics Letters*, vol. 89, no. 26, p. 261503, 2006.

[9] J. Navarro-Cavallé, M. Wijnen, P. Fajardo, and E. Ahedo, "Experimental characterization of a 1 kW helicon plasma thruster," *Vacuum*, vol. 149, pp. 69–73, 2018.

[10] K. Takahashi, "Helicon–type radiofrequency plasma thrusters and magnetic plasma nozzles," *Reviews of Modern Plasma Physics*, vol. 3, p. 3, 2019.

[11] H. Kosmahl, D. Miller, and G. Bethke, "Plasma acceleration with microwaves near cyclotron resonance," *Journal of Applied Physics*, vol. 38, no. 12, pp. 4576–4582, 1967.

[12] J. Sercel, "Electron-cyclotron-resonance (ECR) plasma thruster research," in *24th Joint Propulsion Conference*, no. AIAA 1988-2916, American Institute of Aeronautics and Astronautics, Reston, VA, 1988.

[13] M. R. Inchingolo, M. Merino, and J. Navarro-Cavallé, "Plume characterization of a waveguide ecr thruster," *Journal of Applied Physics*, vol. 133, no. 11, p. 113304, 2023.

[14] V. Désangles, D. Packan, J. Jarrige, S. Peterschmitt, P. Dietz, S. Scharmann, K. Holste, and P. J. Klar, "ECRA thruster advances: 30w and 200w prototypes latest performances," *Journal of Electric Propulsion*, vol. 2, no. 1, p. 10, 2023.

[15] S. Andersen, V. Jensen, P. Nielsen, and N. D'Angelo, "Continuous supersonic plasma wind tunnel," *Phys. Fluids*, vol. 12, no. 3, pp. 557–560, 1969.

[16] R. Gerwin, G. Marklin, A. Sgro, and A. Glasser, "Characterization of plasma flow through magnetic nozzles," Tech. Rep. AFSOR AL-TR-89-092, Los Alamos National Laboratory, 1990.

[17] E. Ahedo and M. Merino, "Two-dimensional supersonic plasma acceleration in a magnetic nozzle," *Physics of Plasmas*, vol. 17, no. 7, p. 073501, 2010.

[18] M. Merino and E. Ahedo, "Magnetic nozzles for space plasma thrusters," in *Encyclopedia of Plasma Technology* (J. L. Shohet, ed.), vol. 2, pp. 1329–1351, Taylor and Francis, 2016.

[19] A. Morozov, Y. Esipchuk, G. Tilinin, A. Trofimov, Y. Sharov, and G.Y.Shchepkin, "Plasma accelerator with closed electron drift and extended acceleration zone," *Soviet Physics-Tech. Physics*, vol. 17, no. 1, pp. 38–45, 1972.

[20] A. Smolyakov, O. Chapurin, W. Frias, O. Koshkarov, I. Romadanov, T. Tang, M. Umansky, Y. Raitses, I. Kaganovich, and V. Lakhin, "Fluid theory and simulations of instabilities, turbulent transport and coherent structures in partially-magnetized plasmas of ExB discharges," *Plasma Physics and Controlled Fusion*, vol. 59, no. 1, p. 014041, 2017.

[21] J. J. Ramos, E. Bello-Benítez, and E. Ahedo, "Local analysis of electrostatic modes in a two-fluid E x B plasma," *Physics of Plasmas*, vol. 28, no. 5, p. 052115, 2021.

[22] M. Ripoli, E. Ahedo, and M. Merino, "Drift-gradient instabilities in a plasma with 2D gradient effects: Application to a magnetic nozzle," *Physics of Plasmas*, vol. 32, p. 092113, 09 2025.

[23] N. A. Krall and P. C. Liewer, "Low-frequency instabilities in magnetic pulses," *Physical Review A*, vol. 4, no. 5, pp. 2094–2103, 1971.

[24] T. Carter, M. Yamada, H. Ji, R. Kulsrud, and F. Trintchouk, "Experimental study of lower-hybrid drift turbulence in a reconnecting current sheet," *Physics of Plasmas*, vol. 9, no. 8, pp. 3272–3288, 2002.

[25] J. J. Ramos and M. Ripoli, "Kinetic theory of drift-gradient modes in a partially magnetised ExB plasma," *Journal of Plasma Physics*, vol. 92, no. 1, p. E12, 2026.

[26] R. Davidson and N. Gladd, "Anomalous transport properties associated with the lower-hybrid-drift instability," *The Physics of Fluids*, vol. 18, no. 10, pp. 1327–1335, 1975.

[27] J. D. Huba and C. S. Wu, "Effects of a magnetic field gradient on the lower hydrid drift instability," *Physics of Fluids*, vol. 19, no. 7, pp. 988–994, 1976.

[28] Y. Sakawa, C. Joshi, P. Kaw, F. Chen, and V. Jain, "Excitation of the modified Simon–Hoh instability in an electron beam produced plasma," *Physics of Fluids B: Plasma Physics*, vol. 5, no. 6, pp. 1681–1694, 1993.

[29] A. Simon, "Instability of a partially ionized plasma in crossed electric and magnetic fields," *The Physics of Fluids*, vol. 6, no. 3, pp. 382–388, 1963.

[30] V. I. Sotnikov, V. D. Shapiro, and V. I. Shevchenko, "Nonlinear theory of the current instability of short-wavelength drift oscillations," *Sov. Phys. - JETP (Engl. Transl.); (United States)*, vol. 51:2, 02 1980.

[31] M. Malkov and V. Sotnikov, "Lower hybrid drift instability and reconnection of magnetic lines of force," *Fizika Plazmy*, vol. 11, pp. 1096–1105, 1985.

[32] T. Lafleur, S. Baalrud, and P. Chabert, "Theory for the anomalous electron transport in Hall effect thrusters. ii. kinetic model," *Physics of Plasmas*, vol. 23, p. 053503, 2016.

[33] G. Hagelaar and G. Kroesen, "Speeding up fluid models for gas discharges by implicit treatment of the electron energy source term," *Journal of Computational Physics*, vol. 159, no. 1, pp. 1–12, 2000.

[34] D. Poli and E. Ahedo, "Full-fluid modelling of rotating plasma instabilities in penning-like configurations," *Plasma Sources Science and Technology*, vol. 35, p. 015007, 01 2026.

[35] C. Birdsall and D. Fuss, "Clouds-in-clouds, clouds-in-cells physics for many-body plasma simulation," *Journal of Computational Physics*, vol. 135, no. 2, pp. 141–148, 1997.

[36] A. Marín-Cebrián, E. Bello-Benítez, A. Domínguez-Vázquez, and E. Ahedo, "Non-maxwellian electron effects on the macroscopic response of a Hall thruster discharge from an axial–radial kinetic model," *Plasma Sources Science and Technology*, vol. 33, p. 025008, 2 2024.

[37] L. Garrigues, I. Boyd, and J. Boeuf, "Computation of Hall thruster performance," *Journal of Propulsion and Power*, vol. 17, no. 4, pp. 772–779, 2001.

[38] M. Guaita, E. Ahedo, and M. Merino, "Pic/fluid simulations of the plasma expansion in a planar magnetic arch," *Plasma Sources Science and Technology*, vol. 34, p. 015007, 1 2025.

[39] E. Bello-Benítez, A. Marín-Cebrián, and E. Ahedo, "Effect of injection conditions on the non-linear behavior of the ECDI and related turbulent transport," *Physics of Plasmas*, vol. 32, no. 1, p. 012307, 2025.

[40] C.-K. Huang, Y. Zeng, Y. Wang, M. Meyers, S. Yi, and B. Albright, "Finite grid instability and spectral fidelity of the electrostatic particle-in-cell algorithm," *Computer Physics Communications*, vol. 207, pp. 123–135, 2016.

[41] G. Lapenta, "Exactly energy conserving semi-implicit particle in cell formulation," *Journal of Computational Physics*, vol. 334, pp. 349–366, 2017.

[42] P. Jiménez, L. Chacón, and M. Merino, "An implicit, conservative electrostatic particle-in-cell algorithm for paraxial magnetic nozzles," *Journal of Computational Physics*, vol. 502, p. 112826, 2024.

[43] T. Charoy, J. P. Boeuf, A. Bourdon, J. A. Carlsson, P. Chabert, B. Cuenot, D. Eremin, L. Garrigues, K. Hara, I. D. Kaganovich, A. T. Powis, A. Smolyakov, D. Sydorenko, A. Tavant, O. Vermorel, and W. Villafana, "2D axial-azimuthal particle-in-cell benchmark for low-temperature partially magnetized plasmas," *Plasma Sources Science and Technology*, vol. 28, no. 10, p. 105010, 2019.

[44] T. Charoy, T. Lafleur, A. Tavant, P. Chabert, and A. Bourdon, "A comparison between kinetic theory and particle-in-cell simulations of anomalous electron transport in ExB plasma discharges," *Physics of Plasmas*, vol. 27, no. 6, p. 063510, 2020.

[45] S. Janhunen, A. Smolyakov, D. Sydorenko, M. Jimenez, I. Kaganovich, and Y. Raitses, "Evolution of the electron cyclotron drift instability in two-dimensions," *Physics of Plasmas*, vol. 25, no. 8, p. 082308, 2018.

[46] W. Villafana, F. Petronio, A. Denig, M. Jimenez, D. Eremin, L. Garrigues, F. Taccogna, A. Alvarez-Laguna, J. Boeuf, A. Bourdon, P. Chabert, T. Charoy, B. Cuenot, K. Hara, F. Pechereau, A. Smolyakov, D. Sydorenko, A. Tavant, and O. Vermorel, "2D radial-azimuthal particle-in-cell benchmark for ExB discharges," *Plasma Sources Science and Technology*, vol. 30, no. 7, p. 075002, 2021.

[47] F. I. Parra, E. Ahedo, J. M. Fife, and M. Martínez-Sánchez, "A two-dimensional hybrid model of the Hall thruster discharge," *Journal of Applied Physics*, vol. 100, no. 2, p. 023304, 2006.

[48] J. Perales-Díaz, A. Domínguez-Vázquez, P. Fajardo, E. Ahedo, F. Faraji, M. Reza, and T. Andreussi, "Hybrid plasma simulations of a magnetically shielded Hall thruster," *Journal of Applied Physics*, vol. 131, no. 10, p. 103302, 2022.

[49] K. Matyash, R. Schneider, A. Mutzke, O. Kalentev, F. Taccogna, N. Koch, and M. Schirra, "Kinetic simulations of spt and hemp thrusters including the near-field plume region," *IEEE Transactions on Plasma Science*, vol. 38, no. 9, pp. 2274–2280, 2010.

[50] L. Lewerentz, D. Kahnfeld, N. Schulz, R. Heidemann, and R. Schneider, "PIC Simulations of the MS4 Thruster," *Frontiers in Physics*, vol. Volume 10 - 2022, 2022.

[51] F. Taccogna, R. Schneider, S. Longo, and M. Capitelli, "Kinetic simulations of a plasma thruster," *Plasma Sources Science and Technology*, vol. 17, no. 2, p. 024003, 2008.

[52] M. Guaita, K. Keil, K. Holste, P. J. Klar, E. Ahedo, and M. Merino, "Numerical and experimental study of facility effects on a gridded ion engine's plasma plume," *Journal of Applied Physics*, vol. 139, p. 093301, 02 2026.

[53] S. Jalas, I. Dornmair, R. Lehe, H. Vincenti, J.-L. Vay, M. Kirchen, and A. R. Maier, "Accurate modeling of plasma acceleration with arbitrary order pseudo-spectral particle-in-cell methods," *Physics of Plasmas*, vol. 24, p. 033115, 03 2017.

[54] C. N. Shen, A. Cerfon, and S. Muralikrishnan, "A particle-in-fourier method with semi-discrete energy conservation for non-periodic boundary conditions," *Journal of Computational Physics*, vol. 519, p. 113390, 2024.

[55] E. Evstatiev and B. Shadwick, "Variational formulation of particle algorithms for kinetic plasma simulations," *Journal of Computational Physics*, vol. 245, pp. 376–398, 2013.

[56] R. Lehe, M. Kirchen, I. A. Andriyash, B. B. Godfrey, and J.-L. Vay, "A spectral, quasi-cylindrical and dispersion-free particle-in-cell algorithm," *Computer Physics Communications*, vol. 203, pp. 66–82, 2016.

[57] M. Kirchen, R. Lehe, S. Jalas, O. Shapoval, J.-L. Vay, and A. R. Maier, "Scalable spectral solver in galilean coordinates for eliminating the numerical cherenkov instability in particle-in-cell simulations of streaming plasmas," *Phys. Rev. E*, vol. 102, p. 013202, Jul 2020.

[58] A. T. Powis, E. Ahedo, A. Álvarez Laguna, N. Barléon, E. Bello-Benítez, L. Beving, J.-P. Boeuf, G. Bogopolsky, A. Bourdon, F. Cichocki, B. Cuenot, A. Denig, Z. Donkó, P.-Q. Elias, M. P. Encinar, D. Eremin, P. Fajardo, F. Faraji, G. Fubiani, L. Garrigues, K. Hara, P. Hartmann, M. Hopkins, I. D. Kaganovich, A. Knoll, G. Lapenta, T. E. Magin, A. Marín-Cebrián, M. Merino, P. Minelli, M. Papahn Zadeh, P. Parodi, F. Petronio, M. Reza, A. I. Smolyakov,

D. Sydorenko, F. Taccogna, M. M. Turner, O. Vermorel, W. Villafana, and L. Xu, "Benchmark for two-dimensional large scale coherent structures in partially magnetized $E \times B$ plasmas—community collaboration & lessons learned," *Plasma Sources Science and Technology*, vol. 35, p. 025002, Feb. 2026.

[59] B. Bayón-Buján, E. Bello-Benítez, J. Zhou, and M. Merino, "Data-Driven Analysis of Anomalous Transport and Three-Wave-Coupling Effects in an E×B Plasma," *Journal of Electric Propulsion*, vol. 4, no. 58, pp. 1–23, 2025.

[60] A. Marín-Cebrián, E. Ahedo, and A. Domínguez-Vázquez, "Two-dimensional kinetic analysis of a Hall thruster discharge with a null-magnetic point at the anode," *Journal of Physics D: Applied Physics*, vol. 58, p. 375201, 09 2025.

[61] M. Guaita, A. Marín-Cebrián, M. Merino, E. Ahedo, F. Cipriani, and K. Dannenmayer, "Electron populations and neutralization process in the plume of a gridded ion thruster," *Plasma Sources Science and Technology*, 3 2025.

[62] "oneMKL PARDISO - Parallel Direct Sparse Solver Interface." `https://www.intel.com/content/www/us/en/docs/onemkl/developer-reference-c/2023-1/onemkl-pardiso-parallel-direct-sparse-solver-iface.html`. Accessed: 2023.

[63] G. Delzanno and E. Camporeale, "On particle movers in cylindrical geometry for Particle-In-Cell simulations," *Journal of Computational Physics*, vol. 253, pp. 259–277, 2013.

[64] R. Ringle, "3DCylPIC—a 3D particle-in-cell code in cylindrical coordinates for space charge simulations of ion trap and ion transport devices," *International Journal of Mass Spectrometry*, vol. 303, no. 1, pp. 42–50, 2011.

[65] M. S. Mitchell, M. T. Miecnikowski, G. Beylkin, and S. E. Parker, "Efficient fourier basis particle simulation," *Journal of Computational Physics*, vol. 396, pp. 837–847, 2019.